Investigation Of Alkaline Solution Temperature Increment Influence Onto SS316L Surface

Basori[1*], Wan Mohd Farid Wan Mohamad[2,3], Noreffendy Tamaldin[2,3], Muhd Ridzuan Mansor[2,3], Maman Kartaman Ajiriyanto[4], Arif Nugroho[4], Rosika Kriswarini[4], Juan Carlos Sihotang[4], Sigit Dwi Yudanto[5], Cahaya Rosyidan[6], and Ferry Budhi Susetyo[7]

[1] *Department of Mechanical Engineering, Universitas Nasional, 12520, Indonesia*
[2] *Faculty of Mechanical Technology and Engineering, Universiti Teknikal Malaysia Melaka, Hang Tuah Jaya, 76100 Durian Tunggal, Melaka, Malaysia*
[3] *Centre for Advanced Research on Energy, Universiti Teknikal Malaysia Melaka, Hang Tuah Jaya, 76100 Durian Tunggal, Melaka, Malaysia*
[4] *Research Center for Nuclear Material and Radioactive Waste Technology - National Research and Innovation Agency, 15314, Indonesia*
[5] *Research Center for Metallurgy - National Research and Innovation Agency, 15314, Indonesia*
[6] *Department of Petroleum Engineering, Universitas Trisakti, 11440, Indonesia*
[7] *Department of Mechanical Engineering, Universitas Negeri Jakarta, 13220, Indonesia*
[*] *Corresponding author. E-mail: basori@civitas.unas.ac.id*

Received: August 15, 2024; Accepted: December 23, 2024

This study deals with the electrochemical behaviors of SS316L at various temperatures in a 3M KOH solution. The mounted SS316L was subjected to electrochemical measurement using a Potentiostat with an exposure area of 1 cm^2. Following electrochemical measurements, the samples were analyzed with a Scanning electron microscope equipped with Energy dispersive spectroscopy (SEM-EDS) to observe the surface morphology and element distribution. Identifying the phases present in the samples is done through X-ray diffraction (XRD). On the basis of SEM images, the surface roughness was also examined. According to OCP investigations, only the lowest solution temperature sample (30 °C) show that they are moving forward in a positive direction. Shifting to a higher solution temperature (from 30 to 50 °C) led to an increase in passive current density according to LSV oxidation measurement. The lowest solution temperature sample (30 °C) shows the lowest corrosion rate and a higher capacitive arc. In contrast, higher hydrogen production is seen in the highest solution temperature sample (50 °C). Moreover, all samples shows p-type and n-type semiconducting properties. According to EDS measurements, the Mn element was not detected in all samples after the electrochemical test due to was sacrificing during corrosion occurs. All samples contain face-centered cubic (fcc)-austenite $(\gamma - \text{Fe})$ as its main phase. The surface of SS316L did not show any oxides to form, probably due to an excessively thin or nanoscale oxide layer on the surface.

Keywords: Electrochemical behavior; Semiconducting; Surface morphology; Element; Structure

http://dx.doi.org/10.6180/jase.202510_28(10).0010

---

1. Introduction

The demand for clean energy demand will increase in the future due to the need for environmentally friendly fuel [1, 2]. Recently, hydrogen has been known as a renewable and clean energy supply and is considered by many studies as the perfect eco-friendly fuel due to its nontoxic [3]. Besides that, hydrogen could be used as a single or mixed with fossil fuels in automotive combustion chambers [4, 5].

Hydrogen production could be produced using an electrolysis process [6]. The electrolysis process was performed with various electrodes, including stainless steel (SS)316L, SS 304, and copper (Cu). SS316L has proven to have better corrosion resistance than the materials mentioned above [7]. The high corrosion resistance of SS316L is attributed to the protective passive layer formed on the outermost surface. Cr and Ni are two elements that react with oxygen and introduce a passive layer.

Several salts, such as KOH, NaOH, and NaCl, were chosen and used in the electrolysis solution [8, 9]. The efficiency of hydrogen production using KOH is 90.25 %, while the efficiency of hydrogen production using NaOH is 83.33 % [8]. Moreover, applying higher current during electrolysis could enhance hydrogen production [10]. Unfortunately, a higher current implies electrolyte solution temperature increases and could cause the electrode to overheat, resulting in less efficiency [11]. Moreover, an increase in alkaline concentration also increases the temperature of the electrolyte solution [11]. Furthermore, increasing the concentration of electrolyte solution also has an impact on the corrosion rate [12].

BenSalah et al., [13] in their study, have found that a porous layer would form at higher solution temperatures, which could imply an increased corrosion rate. Another study was conducted by Escrivà-Cerdán et al. [14] found that the passive films over material that is formed at high temperatures should be more defective. While more stable and protective passive layers form at the lower temperatures [15]. According to Krungkarnchana and Kongvarhodom study [16], the oxide on AISI 304 surface are iron (Fe) and chrome (Cr) oxide. Moreover, in previous research, only Cr oxide was shown on the surface of SS316L after a corrosion test in 50 g/l of KOH at 60 °C [17].

This study aims to investigate the electrochemical behaviors of SS316L at various temperatures in 3M KOH solution and provide a comprehensive overview. SS316L was subjected to Open circuit potential (OCP), Linear sweep voltammetry (LSV), Electro impedance spectroscopy (EIS), and Mott Schottky. Hydrogen evolution reaction (HER) phenomena were also investigated and calculated. Subjected samples, after electrochemical measurement, were analyzed using Scanning electron microscopy equipped with Energy dispersive spectroscopy (SEM-EDS) and X-ray diffraction (XRD) to determine surface morphology, elemental composition, and phase.

2. Experimental setup

2.1. Material and experimental setups

In this experiment, SS316L sheet material was utilized with a composition that was comparable to the previous study [12]. The preparation of 3M KOH solution involved using analytical grade KOH from Sigma Aldrich and mixing it with deionized water. Samples were prepared by cleaning using acetone, then electrochemical behavior (OCP, LSV, EIS, and Mott Schottky) was investigated in various solution temperatures (30, 40, and 50 °C) using Potentiostat (Gamry Reference 600) and namely as T-30, T-40, and T-50. The experiment used a hot plate (Stuart) to maintain the electrolyte solution temperature. Afterward, samples were investigated using SEM-EDS (Phenom Pharos) and XRD (PanAlytical EMPYREAN). The SEM result was analyzed using Image-J software to determine the roughness of the material surface.

2.2. Electrochemical measurement

The SS316L sample was cut and then mounted in the epoxy resin, and the left side was open $\left(1\ \mathrm{cm}^2\right)$ for exposure area. Three cell electrode setups were used for electrochemical measurement: SS316L is the working electrode, saturated calomel electrode (SCE) is the reference electrode, and platinum (Pt) is the counter electrode. OCP scan measurements were performed until 1200 s . The OCP voltage data was collected each 0.5 s . LSV oxidation measurement was undertaken using a scan rate of 1mV/s. By the Tafel extrapolation method for LSV data, corrosion potential ($\mathrm{E}_{\mathrm{corr}}$) and corrosion current density ($\mathrm{i}_{\mathrm{corr}}$) could be found, and then, the corrosion rate could be calculated using the following equation [18].

$$CR(mpy) = \frac{CMi_{\mathrm{corr}}}{n\rho} \tag{1}$$

Where CR is corrosion rate (mpy), C is corrosion constant (0.129), M is atomic weight (g/mol), $\mathrm{i}_{\mathrm{corr}}$ is corrosion current density $\left(\mathrm{A/cm^2}\right)$, n is the number of electrons involved, and ρ is the density of SS 316 L $\left(\mathrm{g/cm^3}\right)$.

HER was also investigated using LSV data. HER parameters can be calculated using reduction scan data. Moreover, EIS was measured at OCP between 1200 – 0.2 Hz and alternating signal of 10 mV amplitude. The Moot Schottky was investigated at a frequency of 1000 Hz, and the potential change was from -2 to +1.5 V vs SCE to determine p-type and n-type semiconducting properties.

2.3. Surface morphology, elemental composition, and structure

Following electrochemical measurements, the samples were analyzed with SEM-EDS and XRD. The SEM-EDS apparatus was used to investigate surface morphology and elemental percentages. XRD was investigated ($CuK\alpha\lambda = 0.154$ nm) from 20 to 80° with a step size of 0.02°. The XRD data was analyzed using the Rietveld method associated with the general structure analysis system (GSAS).

3. Result discussions

3.1. Electrochemical Measurement

The results of the OCP measurements are presented in Fig. 1(a). Only T-50 samples presents steady-state OCP voltage at 1200 s. While the T-30 sample is still moving forward in a more positive direction, and the T-40 sample is moving forward in a negative direction, it needs more time to reach a steady state. A rise to a positive direction indicates that oxide has been formed, while a shift to a negative direction suggests the dissolution of the film oxide [19]. Moreover, the T-50 sample at the beginning until 250 s is shifted to a more positive direction, indicating oxide form on the SS316L surface. As immersion time increases, the OCP curve moves to a negative direction at 250 until 1200 s measuring time, indicating that surface oxide is dissolved [20].

According to the Arjmand et al. [21] study, because of the high amount of Cr in the SS 316 L chemical composition, it is expected that Cr_2O_3 will be the dominant compound in the protective oxide layer of the alloy. Moreover, Ni and Fe can also be transformed by passing through the Cr oxide layer, reacting with OH^-, and finally precipitating to form an oxide in the outer layer.

The results of the LSV measurements are presented in Fig. 1(b). All samples show several domains, such as (1) cathodic, (2) active area, (3) passive area, (4) transpassive area, and (5) oxygen evolution. Escrivà-Cerdán et al. [14] stated that passive films over material that is formed at high temperatures should be more defective. Hence, it consequently accelerates the dissolution of aggressive ion species in the passive layer into electrolyte solution [22]. Moreover, changing the solution temperature from 30 to 40 or 50°C promoted the shift of corrosion potential to more negative potential, attributed to the anodic process acceleration [23].

Increasing the solution temperature leads to a shift in the right-hand direction of the LSV curve, which is in perfect agreement with the study by Monteiro et al. [24]. Yang et al. [25] study also showed similar behavior, investigating SS316L in H_2SO_4 using temperatures 25, 50, 70, and 90°C, showing an LSV curve shift to the right-hand direction with an increase in the solution temperature. Moreover, there is a correlation between the concentration of solution and the passive region. Based on a previous study, only one passive region was formed when LSV was investigated in 5, 30, and 50 g/1 of KOH [17].

According to Fig. 1(b), the Tafel extrapolation method was used to fit the curve to find the E_{corr} and i_{corr}, which were by inserting the i_{corr} in Eq. (1), corrosion rate (CR) was found and summarized in Table 1.

According to Table 1, higher solution temperature led to an increase in corrosion rates. This is probably due to a higher passive current density, as shown in Fig. 1(b). According to a study by Monteiro et al. [24], passive current density depends on the corrosion rate. Therefore, there is a rise in the corrosion rate due to higher passive current density. Another possibility is that the passive film over the surface material formed at high temperatures is more defective [14]; therefore, higher solution temperature increases the corrosion rate.

Moreover, compared to the OCP curve, only T-30 has moved in a positive direction, which means that it has formed a protective oxide form and has resulting high corrosion resistance. Generally, all samples show excellent corrosion resistance criteria due to a corrosion rate value between 1-5 mpy [26].

The results of the EIS measurements are presented in Fig. 1(c) and (d). According to Fig. 1 (c), capacitive arcs are formed in the various samples. A high capacitive arc is related to lower metal dissolution, and the diameter of the capacitive arc is related to charge transfer resistance (Rct) [27]. In other words, a higher capacitive arc is near the highest corrosion resistance. Wang et al. [23] have found that the corrosion rate of the stainless steel is mainly controlled by the anodic stage. Therefore, the decrease in capacitive arc diameter indicates an increase in the anodic reaction rate. Compared to corrosion parameter (Table 1), the T-30 sample has a lower corrosion rate due to a higher capacitive arc.

According to Fig. 1(d), the T-30 sample has a phase angle close to -75° at an intermediate frequency, which indicates that it has more stable and protective passive layers than other samples [15]. Compared to Fig. 1(b), it can be seen that a narrow passive layer is seen in the T-30 sample, while the T-40 and T-50 samples are wider. Unfortunately, the wider passive layer in the T-40 and T-50 samples has poor stability, resulting in a higher corrosion rate than the T-30 sample. The passive layer in the T-40 and T-50 samples probably contains Fe oxides, which results in poor passive

Table 1. Corrosion and EIS parameters.

Sample	Corrosion Parameters			EIS Parameters	
	$\mathbf{E_{corr}}$ $(\mathbf{V})$ vs SCE	$\mathbf{i_{corr}}$ $(\mathbf{A/cm^2})$	CR (mpy)	Rs $(\mathbf{\Omega})$	Rct $(\mathbf{\Omega})$
T-30	-0.357	2.670×10^{-6}	1.186	10.50	3.63×10^3
T-40	-0.554	3.740×10^{-6}	1.662	15.53	3.51×10^3
T-50	-0.514	3.840×10^{-6}	1.707	19.25	1.19×10^3

layer stability. Moreover, various EIS parameters can be found and presented in Table 1 by fitting the curve using an electrical equivalent circuit (EEC) diagram [28].

According to Table 1 (EIS parameters), the solution resistance (Rs) and charge transfer resistance (Rct) values decrease by increasing the solution temperature and are in perfect agreement with the LSV result. This condition means Rs and Rct are dependent on the solution temperature. Previous research found that a decrease in the Rct leads to a rise in the corrosion rate of SS316L [12]. Hossain et al. [28] also found similar behavior; a reduction in Rct promoted a decrease in corrosion resistance in the alloy. Mott Schottky's measurement result is presented in Fig. 1 (e). All samples show p-type and n-type region behaviors. Moreover, all samples have 0.5 V vs SCE turning potential. Less than 0.5 V vs SCE (first region) is attributed to p-type, and more than 0.5 V vs SCE (second region) is attributed to n-type [12]. Several studies were investigated in various temperatures, focusing on a positive direction [29, 30]; therefore, the present study also focused on a positive direction.

The potential around 0 to +5 V vs SCE represents p-type. Meanwhile, the potential around +5 to +1.5 V vs SCE represents the n-type. Cr_2O_3 is forming at flat band potential of p-type. Moreover, Cr_2O_3 and NiO form at an initial or lower potential of n -type, and then Fe_2O_3 forms at the higher potential of n-type [31–33].

3.2. Hydrogen Evolution Reaction (HER)

The results of the cathodic scan measurements are presented in Fig. 2(a). The T-30 sample suggests the smallest onset potential, whereas the T-50 suggests the highest. In the present study, the onset potential is dependent on the solution temperature. Increasing the solution temperature promoted a decrease in the onset potential. Ng et al. [34] stated that small onset potential indicates higher HER activation energy.

At the cathode, the electrochemical response in alkaline and acidic electrolytes is referred to as the HER. The electrochemical reaction for alkaline and acidic electrolytes is as follows [35–37].

$$2H_2O + 2e^- \rightarrow H_2 + 2OH^- \quad (2)$$

$$2H^+ + 2e^- \rightarrow H_2 \quad (3)$$

Linear regression using Eq. (4) was used to fit the Tafel plot in Fig. 2(b) [38]. Meanwhile, the exchange current density was calculated using Eq. (5) and summarize in Table 2 [38].

$$\eta = a + b \log J_0 \quad (4)$$

$$\log (J_0) = -\frac{a}{b} \quad (5)$$

Where η is the overpotential (V), a is the Tafel intercept, b is the Tafel slope, and J_0 is the exchange current density (A/cm^2).

Table 2. HER kinetic parameter of samples.

Sample	$\mathbf{a(V)}$	$\mathbf{b(V/dec)}$	$\eta\mathbf{(V)}$	$\mathbf{J_0}$ $(\mathbf{A/cm^2})$
T-30	-0.388	0.1066	-0.417	4362.896
T-40	-0.383	0.0995	-0.407	7067.181
T-50	-0.410	0.1056	-0.402	7630.900

According to Huang et al. [39], the higher the exchange current density (J_0), the more hydrogen gas is produced. Therefore, the T-50 sample has higher gas production than other samples. Moreover, El Soly et al. [11] have investigated hydrogen production using dry and wet cells using various solution temperatures and found that an increase in temperature leads to resulting high flowrate hydrogen production.

3.3. Scanning Electron Microscopy - Energy Dispersive Spectroscopy (SEM-EDS)

The results of the SEM-EDS investigations are presented in Fig. 3. The grain boundaries of various samples can be clearly seen. This behavior probably causes corrosion to occur at grain boundaries. Moreover, several holes were also seen in all samples, which indicates that all samples experienced pitting corrosion. Therefore, it can be concluded that there were two types of corrosion present in all samples.

Previous research, when investigating SS316L in various KOH concentrations, found corrosion in grain boundaries [12]. Moreover, Oh et al. [40] found that pitting corrosion occurred on SS after the potentiodynamic polarization (LSV) test.

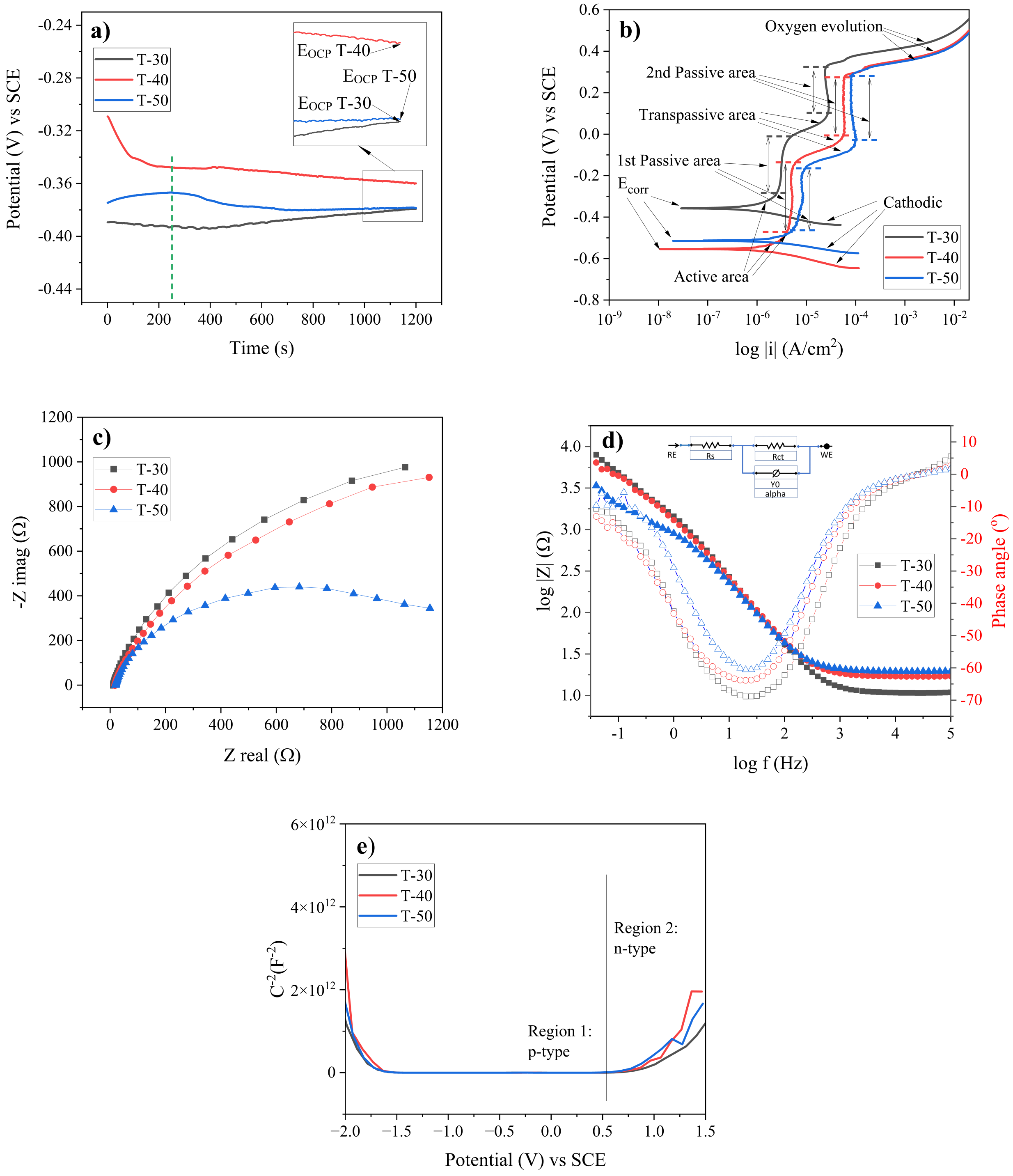

Fig. 1. Electrochemical measurement result (a) OCP, (b) LSV (c) EIS-Nyquist impedance plot, (d) EIS-Bode plot, and (e) Mott Schottky.

The results of the surface roughness investigations using SEM pictures are presented in Fig. 4. The surface roughness of T-30, T-40, and T-50 is 18.96, 24.63 and 25.52 µm respectively. Therefore, it can be concluded that a rise in the corrosion rate increases the surface roughness of the sample, which perfectly agrees with the study by Toloei et al. [41].

According to the EDS investigation, sample elements

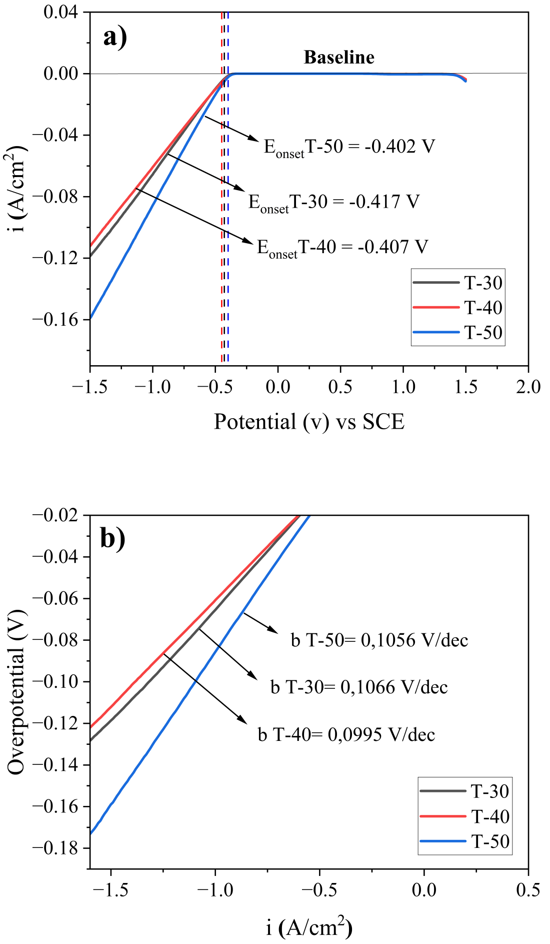

Fig. 2. HER investigation (a) Cathodic scan measurement result and (b) Tafel plot of samples.

can be seen in Table 3.

Table 3. Elements of sample according to EDS investigation.

Sample Name	Weight Conc. (wt.%)				
	Fe	Cr	Ni	O	Mo
T-30	69.78	13.98	10.65	2.98	2.62
T-40	69.36	13.97	10.58	3.10	2.99
T-50	69.10	14.06	10.64	3.21	2.99

The chemical composition of the SS316L is Cr 16.33 wt.%, Ni 9.97 wt.%, Mn 2.06 wt. %, Mo 1.95 wt. %, and Fe balance [12]. Compared to Table 3, the Mn element is not seen after the electrochemical test. According to Cihangir et al. [42], Mn disappears after the electrochemical test due to was sacrificing during corrosion occurs. This behavior was also found in the study by Ni et al. [43], who investigated the corrosion of SS314 in molten carbonate. In their study, Choudhary et al. [44] found that Mn's dissolution rate is higher than Fe, Ni, Mo and Cr; therefore, Mn disappears after the electrochemical test.

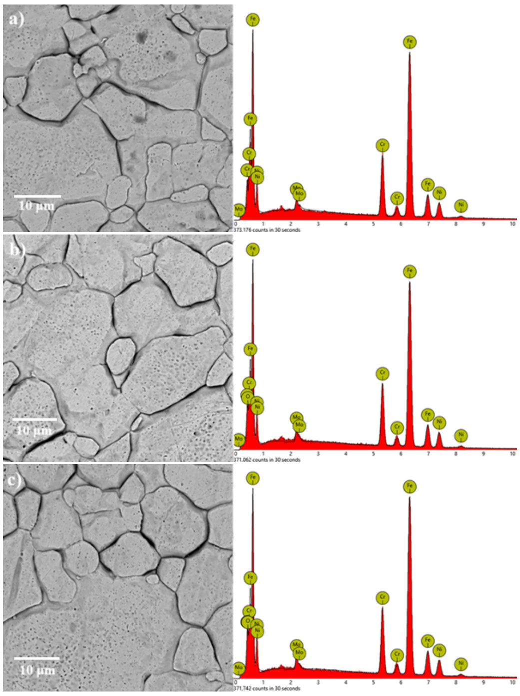

Fig. 3. SEM-EDS of samples (a) T-30, (b) T-40, and (c) T-50.

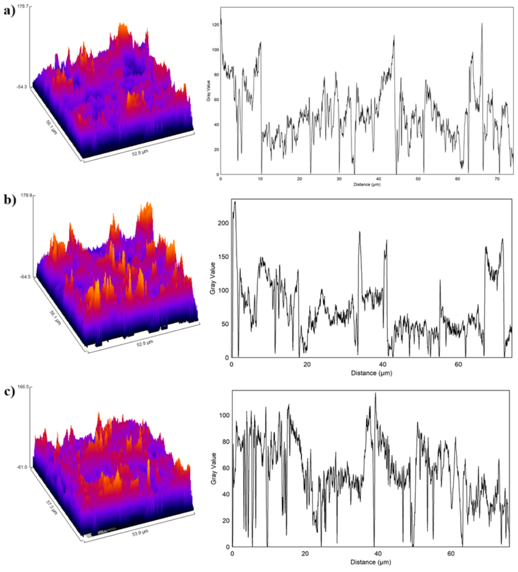

Fig. 4. 3D SEM picture and gray value against distance (left-right) (a) T-30, (b) T-40, and (c) T-50.

According to Table 3, a rise in the solution temperature leads to an increase in oxygen. This condition is probably due to more oxides being formed on sample surfaces by increasing the solution temperature. Moreover, oxides are always seen on the specimen surface after the corrosion test [45, 46].

3.4. XRD

The XRD scan measurement result for three samples can be seen in Fig. 5. The reflections of the (111), (200), and (220) plane diffraction patterns for samples T-30, T-40, and T-50 confirmed the presence of a face-centered cubic (fcc)-austenite (γ-Fe). These austenite phase peaks are comparable to those observed in research conducted by Santamaria, et al. [47]. In addition to the austenite phase, a body-centered cubic (bcc)-ferrite ($\alpha - \text{Fe}$) phase can also be seen at 44.71°. Furthermore, Santamaria and co-authors confirmed that the ferrite phase peak found at this angle aligns with the austenite phase present in SS316 [47]. The surface of SS316 did not show any oxides to form when exposed to a KOH solution heated to 30, 40, and 50°C. These findings correspond to those from an earlier study [12]. This could be due to an excessively thin or nanoscale oxide layer on the surface of SS316L.

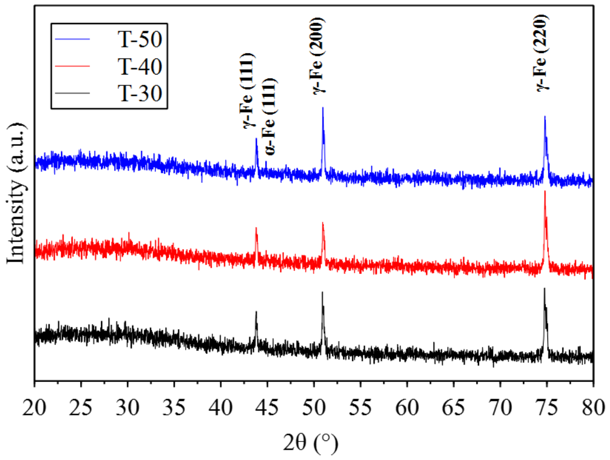

Fig. 5. Location of the KVMRT project

The quantitative analysis of diffraction patterns revealed that the austenite phase formed for almost 98 wt.% of the investigated phases. The lattice constants of the bcc-ferrite phase (im-3m) and the fcc-austenite phase (fm-3m) are 0.287 nm and 0.359 nm, respectively. According to this calculation, the lattice constant value of the bcc-ferrite phase is comparable to the findings that were published in several reports [48, 49]. The lattice constant values for the fcc-austenite phase are consistent with those reported by Lobodyuk et al. [50].

4. Conclusions

An electrochemical investigation of SS316L in various alkaline solution temperatures has been conducted. Several investigations after electrochemical tests, such as SEM-EDS and XRD, were also undertaken. Only the lowest solution temperature sample (30 °C) showed OCP voltage moving forward positively, which indicates a protective oxide form and results in high corrosion resistance. Moreover, rising the solution temperature (from 30 to 50 °C) led to an increase in corrosion rate and hydrogen production. A lower corrosion rate is seen in the lowest solution temperature sample (30 °C) due to the smallest passive current density, higher capacitive arc, lowest charge transfer resistance, and lowest solution resistance. In contrast, higher hydrogen production is seen in the highest solution temperature sample (50 °C) due to the higher exchange current density and the smaller the overpotential. According to several investigations in the present study, SS316L is recommended as an electrode in hydrogen gas production due to its excellent corrosion resistance criteria.

References

[1] X. An, Q. Zhao, and X. Li, (2024) *"Feasibility Study of Using Industrial Wind Turbine in Manjil City by Energy, Exergy, Economic and Exergy Destruction Analysis"* **Journal of Applied Science and Engineering *27***: 2713–2723. DOI: 10.6180/jase.202406_27(6).0011.

[2] K. B. M. Kiran, M. S. Indira, and R. Nagaraja, (2022) *"Mathematical Modeling and Evaluation of Performance Characteristics of a Hybrid Solar PV and Wind Energy System"* **Journal of Applied Science and Engineering *25***: 785–797. DOI: 10.6180/jase.202208_25(4).0014.

[3] F. Dawood, M. Anda, and G. Shafiullah, (2020) *"Hydrogen Production for Energy: An Overview"* **International Journal of Hydrogen Energy *45***: 3847–3869. DOI: 10.1016/j.ijhydene.2019.12.059.

[4] I. Puspitasari, N. Wahyudi, Y. A. Fakhrudi, and G. P. Wicaksono, (2021) *"Design of Generator HHO Dry Cell Type and Application on 110 CC Engined Vehicles Towards Gas Emissions"* **Journal of Physics: Conference Series *1845***: 012002. DOI: 10.1088/1742-6596/1845/1/012002.

[5] S. A. Musmar and A. A. Al-Rousan, (2011) *"Effect of HHO Gas on Combustion Emissions in Gasoline Engines"* **Fuel *90***: 3066–3070. DOI: 10.1016/j.fuel.2011.05.013.

[6] C.-W. Sun and S.-S. Hsiau, (2018) *"Effect of Electrolyte Concentration Difference on Hydrogen Production During PEM Electrolysis"* **Journal of Electrochemical Science and Technology** ***9***: 99–108. DOI: 10.5229/JECST.2018.9.2.99.

[7] I. Hamidah, A. Solehudin, and A. Setiawan, (2016) *"Effect of Variation of Kalium Hydroxide Solution Concentration and Temperature to the Corrosion Resistance of AISI 304, AISI 316, and Copper Alloys in Water Electrolysis Apparatus"* **ARPN Journal of Engineering and Applied Science** ***11***: 972–977.

[8] M. H. Sellami and K. Loudiyi, (2017) *"Electrolytes Behavior during Hydrogen Production by Solar Energy"* **Renewable and Sustainable Energy Reviews** ***70***: 1331–1335. DOI: 10.1016/j.rser.2016.12.034.

[9] A. Budiman, M. Yerizam, and Y. Bow, (2021) *"Design of Dry Cell HHO Generator using NaCl Solution for Hydrogen Production"* **Indonesian Journal of Fundamental And Applied Chemistry (IJFAC)** ***7***: 8–15. DOI: 10.24845/ijfac.v7.i1.8.

[10] A. B. Vethamony and V. Thangavel, (2023) *"Experiments on the Effect of Temperature on HHO Production by Alkaline Water Electrolysis"* **Materials Today: Proceedings**: DOI: 10.1016/j.matpr.2023.03.771.

[11] A. El Soly, M. El Kady, A. E. F. Farrag, and M. Gad, (2021) *"Comparative Experimental Investigation of Oxyhydrogen (HHO) Production Rate using Dry and Wet Cells"* **International Journal of Hydrogen Energy** ***46***: 12639–12653. DOI: 10.1016/j.ijhydene.2021.01.110.

[12] B. Basori, W. M. Mohamad, M. R. Mansor, N. Tamaldin, A. Iswandi, M. K. Ajiriyanto, and F. B. Susetyo, (2023) *"Effect of KOH Concentration on Corrosion Behavior and Surface Morphology of Stainless Steel 316L for HHO Generator Application"* **Journal of Electrochemical Science and Engineering** ***13***: 451–467. DOI: 10.5599/jese.1615.

[13] M. BenSalah, R. Sabot, E. Triki, L. Dhouibi, P. Refait, and M. Jeannin, (2014) *"Passivity of Sanicro28 (UNS N-08028) Stainless Steel in Polluted Phosphoric Acid at Different Temperatures Studied by Electrochemical Impedance Spectroscopy and Mott-Schottky Analysis"* **Corrosion Science** ***86***: 61–70. DOI: 10.1016/j.corsci.2014.04.056.

[14] C. Escrivà-Cerdán, E. Blasco-Tamarit, D. M. García-García, J. García-Antón, and A. Guenbour, (2012) *"Passivation Behaviour of Alloy 31 (UNS N08031) in Polluted Phosphoric Acid at Different Temperatures"* **Corrosion Science** ***56***: 114–122. DOI: 10.1016/j.corsci.2011.11.014.

[15] Z. Wang, Z. Feng, and L. Zhang, (2020) *"Effect of High Temperature on the Corrosion Behavior and Passive Film Composition of 316 L Stainless Steel in High H2S-containing Environments"* **Corrosion Science** ***174***: 108844. DOI: 10.1016/j.corsci.2020.108844.

[16] H. Krungkarnchana and C. Kongvarhodom, (2019) *"Low Temperature Corrosion: Oxidation of Carbon Steel and Stainless Steel in Air"* **Applied Science and Engineering Progress** ***12***: 44–51. DOI: 10.14416/j.ijast.2018.05.001.

[17] B. Basori, W. Mohamad, N. Tamaldin, M. Mansor, M. Ajiriyanto, S. Yudanto, and F. Susetyo, (2023) *"Influence of Temperature and Azithromycin on the Surface of SS 316L in a KOH Solution"* **International Journal of Corrosion and Scale Inhibition** ***12***: 258–274. DOI: 10.17675/2305-6894-2023-12-1-15.

[18] Z. Ahmad, (2006) *"Principles of Corrosion Engineering and Corrosion Control"*: 1–656. DOI: 10.1016/b978-0-7506-5924-6.x5000-4.

[19] M. Talha, C. Behera, and O. Sinha, (2012) *"Potentiodynamic Polarization Study of Type 316L and 316LVM Stainless Steels for Surgical Implants in Simulated Body Fluids"* **Journal of Chemical and Pharmaceutical Research** ***4***: 203–208.

[20] Ž. Z. Tasić, M. B. P. Mihajlović, M. B. Radovanović, and M. M. Antonijević, (2018) *"Electrochemical Investigations of Copper Corrosion Inhibition by Azithromycin in 0.9% NaCl"* **Journal of Molecular Liquids** ***265***: 687–692. DOI: 10.1016/j.molliq.2018.03.116.

[21] F. Arjmand, L. Zhang, and J. Wang, (2017) *"Effect of Temperature, Chloride and Dissolved Oxygen Concentration on the Open Circuit and Transpassive Potential Values of 316L Stainless Steel at High-Temperature Pressurized Water"* **Nuclear Engineering and Design** ***322***: 215–226. DOI: 10.1016/j.nucengdes.2017.06.048.

[22] H. Iken, R. Basseguy, A. Guenbour, and A. B. Bachir, (2007) *"Classic and Local Analysis of Corrosion Behaviour of Graphite and Stainless Steels in Polluted Phosphoric Acid"* **Electrochimica Acta** ***52***: 2580–2587. DOI: 10.1016/j.electacta.2006.09.013.

[23] Z. Wang, L. Zhang, X. Tang, Z.-y. Cui, J.-p. Xue, and M.-x. Lu, (2017) *"Investigation of the Deterioration of Passive Films in H2S-containing Solutions"* **International Journal of Minerals, Metallurgy, and Materials** ***24***: 943–953. DOI: 10.1007/s12613-017-1482-6.

[24] R. D. Monteiro, J. V. D. Wetering, B. Krawczyk, and D. L. Engelberg, (2019) *"Corrosion Behaviour of Type 316L Stainless Steel in Hot Caustic Aqueous Environments"* **Metals and Materials International *26***: 630–640. DOI: 10.1007/s12540-019-00403-2.

[25] Y. Yang, L. Guo, and H. Liu, (2011) *"The Effect of Temperature on Corrosion Behavior of SS316L in the Cathode Environment of Proton Exchange Membrane Fuel Cells"* **Journal of Power Sources *196***: 5503–5510. DOI: 10.1016/j.jpowsour.2011.02.070.

[26] M. Ridha, S. Fonna, S. Huzni, J. Supardi, and A. Ariffin, (2013) *"Atmospheric Corrosion of Structural Steels Exposed in the 2004 Tsunami-affected Areas of Aceh"* **International Journal of Automotive and Mechanical Engineering *7***: 1014–1022. DOI: 10.15282/ijame.7.2012.17.0082.

[27] X.-x. Fang, H.-z. Zhou, and Y.-j. Xue, (2015) *"Corrosion Properties of Stainless Steel 316L/Ni-Cu-P Coatings in Warm Acidic Solution"* **Transactions of Nonferrous Metals Society of China *25***: 2594–2600. DOI: 10.1016/S1003-6326(15)63880-8.

[28] A. Hossain, F. Gulshan, and A. S. W. Kurny, (2015) *"Electrochemical Corrosion Behavior of Ni-containing Hypoeutectic Al-Si Alloy"* **Journal of Electrochemical Science and Engineering *5***: 173–179. DOI: 10.5599/jese.174.

[29] J. Huang, X. Wu, and E.-H. Han, (2009) *"Influence of pH on Electrochemical Properties of Passive Films Formed on Alloy 690 in High Temperature Aqueous Environments"* **Corrosion Science *51***: 2976–2982. DOI: 10.1016/j.corsci.2009.08.002.

[30] T. Dan, T. Shoji, Z. Lu, K. Sakaguchi, J. Wang, E.-H. Han, and W. Ke, (2010) *"Effects of Hydrogen on the Anodic Behavior of Alloy 690 at 60 °C"* **Corrosion Science *52***: 1228–1236. DOI: 10.1016/j.corsci.2009.11.039.

[31] Z. Feng, X. Cheng, C. Dong, L. Xu, and X. Li, (2010) *"Passivity of 316L Stainless Steel in Borate Buffer Solution Studied by Mott–Schottky Analysis, Atomic Absorption Spectrometry and X-ray Photoelectron Spectroscopy"* **Corrosion Science *52***: 3646–3653. DOI: 10.1016/j.corsci.2010.07.013.

[32] N. Hakiki, S. Boudin, B. Rondot, and M. D. C. Belo, (1995) *"The Electronic Structure of Passive Films Formed on Stainless Steels"* **Corrosion Science *37***: 1809–1822. DOI: 10.1016/0010-938X(95)00084-W.

[33] C. Sunseri, S. Piazza, and F. Di Quarto, (1990) *"Photocurrent Spectroscopic Investigations of Passive Films on Chromium"* **Journal of the Electrochemical Society *137***: 2411–2417. DOI: 10.1149/1.2086952.

[34] C. H. Ng, O. Winther-Jensen, C. A. Ohlin, and B. Winther-Jensen, (2015) *"Exploration and Optimisation of Poly(2,2-bithiophene) as a Stable Photo-electrocatalyst for Hydrogen Production"* **Journal of Materials Chemistry A *3***: 11358–11366. DOI: 10.1039/c5ta00291e.

[35] K. Zeng and D. Zhang, (2010) *"Recent Progress in Alkaline Water Electrolysis for Hydrogen Production and Applications"* **Progress in Energy and Combustion Science *36***: 307–326. DOI: 10.1016/j.pecs.2009.11.002.

[36] S. Marini, P. Salvi, P. Nelli, R. Pesenti, M. Villa, M. Berrettoni, G. Zangari, and Y. Kiros, (2012) *"Advanced Alkaline Water Electrolysis"* **Electrochimica Acta *82***: 384–391. DOI: 10.1016/j.electacta.2012.05.011.

[37] W.-X. Chen, (2001) *"Kinetics of Hydrogen Evolution Reaction on Hydrogen Storage Alloy Electrode in Alkaline Solution and Effects of Surface Modification on the Electrocatalytic Activity for Hydrogen Evolution Reaction"* **International Journal of Hydrogen Energy *26***: 603–608. DOI: 10.1016/S0360-3199(00)00119-1.

[38] V. Protsenko, L. Bobrova, T. Butyrina, and F. Danilov, (2019) *"Hydrogen Evolution Reaction on Cr-C Electrocatalysts Electrodeposited from a Choline Chloride Based Trivalent Chromium Plating Bath"* **Voprosy Khimii i Khimicheskoi Tekhnologii**: 61–66. DOI: 10.32434/0321-4095-2019-122-1-61-66.

[39] Y.-g. Huang, H.-l. Fan, Z.-k. Chen, C.-b. Gu, M.-x. Sun, H.-q. Wang, and Q.-y. Li, (2016) *"The Effect of Graphene for the Hydrogen Evolution Reaction in Alkaline Medium"* **International Journal of Hydrogen Energy *41***: 3786–3793. DOI: 10.1016/j.ijhydene.2015.12.113.

[40] S. Oh, D. Kim, K. Kim, D.-I. Kim, W. Chung, and B.-H. Shin, (2023) *"The Effect of Surface Roughness on Re-passivation and Pitting Corrosion of Super Duplex Stainless Steel UNS S 32760"* **International Journal of Electrochemical Science *18***: 100351. DOI: 10.1016/j.ijoes.2023.100351.

[41] A. Toloei, V. Stoilov, and D. Northwood, (2013) *"The Relationship Between Surface Roughness and Corrosion"* **ASME International Mechanical Engineering Congress and Exposition *56192***: V02BT02A054. DOI: 10.1115/IMECE2013-65498.

[42] S. Cihangir, Y. Say, I. Ozkul, O. Guler, and S. H. Guler, (2022) *"Microstructure and Corrosion Investigation of FeCoCrNiMo0,5(MnAl)0,3 High Entropy Alloy Produced by 316 L Stainless Steel Scrap"* **Materials Today Communications *33***: 104360. DOI: 10.1016/j.mtcomm.2022.104360.

[43] C. Ni and L. Lu, (2014) *"Electrochemical Impedance and Modelling Studies of the Corrosion of Three Commercial Stainless Steels in Molten Carbonate"* **International Journal of Corrosion *2014***: 721208. DOI: 10.1155/2014/721208.

[44] S. Choudhary, R. Kelly, and N. Birbilis, (2024) *"On the Origin of Passive Film Breakdown and Metastable Pitting for Stainless Steel 316L"* **Corrosion Science *230***: 111911. DOI: 10.1016/j.corsci.2024.111911.

[45] G. Jiang, D. Xu, J. Liu, J. Yang, Y. Li, and W. Kuang, (2024) *"Corrosion Protection and Failure Mechanism of ZrO2 Coating on Zirconium Alloy Zry-4 under Varied LiOH Concentrations in Lithiated Water at 360 °C/18.5 MPa"* **Applied Surface Science *650***: 159173. DOI: 10.1016/j.apsusc.2023.159173.

[46] G. Jiang, D. Xu, S. Guo, L. Liu, B. Hao, and M. Wang, (2022) *"Corrosion Behavior and Mechanisms of Al2O3 and Mo Coated Zircaloy-4 in High-temperature Lithiated Water"* **Corrosion Science *201***: 110270. DOI: 10.1016/j.corsci.2022.110270.

[47] R. Santamaria, K. Wang, M. Salasi, M. Iannuzzi, M. Y. Mendoza, and M. Z. Quadir, (2023) *"Stress Corrosion Cracking of 316L Stainless Steel Additively Manufactured with Sinter-based Material Extrusion"* **Materials *16***: 4006. DOI: 10.3390/ma16114006.

[48] S.-J. Lee and Y.-K. Lee, (2005) *"Quantitative Analyses of Ferrite Lattice Parameter and Solute Nb Content in Low Carbon Microalloyed Steels"* **Scripta Materialia *52***: 973–976. DOI: 10.1016/j.scriptamat.2005.01.028.

[49] I. Seki and K. Nagata, (2005) *"Lattice Constant of Iron and Austenite Including its Supersaturation Phase of Carbon"* **ISIJ international *45***: 1789–1794. DOI: 10.2355/isijinternational.45.1789.

[50] V. Lobodyuk, Y. Y. Meshkov, and E. Pereloma, (2019) *"On Tetragonality of the Martensite Crystal Lattice in Steels"* **Metallurgical and Materials Transactions A *50***: 97–103. DOI: 10.1007/s11661-018-4999-z.